Physics of Fluids

Aerodynamic performance of a bio-inspired flapping wing with local sweep morphing

Chunyu Wang (王春雨); Yi Liu (刘毅); Duo Xu (徐多); ... et. al

Check for updates

CrossMark

View Online   Export Citation

Articles You May Be Interested In

Propulsion of a combined heaving and trailing-edge morphing foil for bio-inspired applications
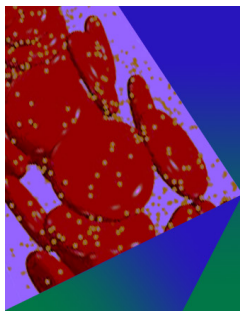
Physics of Fluids (April 2023)

Lift enhancement by dynamically changing wingspan in forward flapping flight

Physics of Fluids (June 2014)

Design and analysis of morphing wing based on different types of wings

AIP Conference Proceedings (November 2022)

Physics of Fluids

Special Topic: Flow and Forensics

Submit Today!

AIP Publishing

AIP Publishing

Aerodynamic performance of a bio-inspired flapping wing with local sweep morphing

View Online　　Export Citation　　CrossMark

Chunyu Wang (王春雨),[1,2] Yi Liu (刘毅),[1,2] Duo Xu (徐多),[1,2] [iD] and Shizhao Wang (王士召)[1,2,a] [iD]

AFFILIATIONS

[1]The State Key Laboratory of Nonlinear Mechanics, Institute of Mechanics, Chinese Academy of Sciences, Beijing 100190, China
[2]School of Engineering Sciences, University of Chinese Academy of Sciences, Beijing 101408, China

Note: This paper is part of the special topic, Flow and Acoustics of Unmanned Vehicles.
[a]Author to whom correspondence should be addressed: wangsz@lnm.imech.ac.cn

ABSTRACT

Birds and bats frequently reconfigure their wing planform through a combination of flapping and local sweep morphing, suggesting a possible approach for improving the performance of micro aerial vehicles. We explore the effects of combined flapping and local sweep morphing on aerodynamic performance by employing a bio-inspired two-jointed flapping wing with local sweep morphing. The bio-inspired wing consists of inner and outer sections, which flap around the root joint (shoulder) and the midspan joint (wrist), respectively. The aerodynamic forces and the unsteady vortex structures are evaluated by numerically solving the incompressible Navier–Stokes equations. The results show that combined flapping and local sweep morphing can significantly enhance the aerodynamic performance. In particular, the average lift coefficient is 1.50 times greater than that of simple gliding with single local sweep morphing. Combined flapping and local sweep morphing also have a relatively high pitch moment and shift the aerodynamic center position backward, producing advantages in terms of maneuverability/agility and stability. We find that the vortex structures associated with the combined motion feature midspan vortices, which arise from the leading-edge vortices of the inner wing and contribute to the enhanced aerodynamic performance. We show that the kinematics of combined flapping and local sweep morphing can be further optimized if the midspan vortices are captured by the outer wing.

I. INTRODUCTION

There has been rising attention to the development of morphing drones for fixed-wing and flapping-wing flights.[1–4] Morphing drones enable radical geometry changes that would improve system capabilities in multiple flight conditions. Morphing wings (part of any morphing drone) are of particular interest because the morphing operation tends to produce nontrivial performance enhancements. The aerodynamic design of morphing wings requires an innovative reconfiguration of the internal structure and external flow.[2] It is equally important to explore the mechanism by which the novel morphing drives the flow toward the optimal aerodynamic performance.

The inspiration for morphing wings comes from natural flyers. According to the constitution of the wing geometry, the morphing can be categorized as two-dimensional airfoil-level morphing or three-dimensional wing-level morphing.[1,5] The airfoil-level morphing refers to alterations to the thickness and camber of the cross-sectional profile, while the wing-level morphing involves spanning, twisting, bending, and sweeping transformations.[1] The morphing of the wing might notably increase the strength and stability of the attached vortex

structures, such as the leading-edge vortex (LEV),[6,7] especially when the drone requires high levels of maneuverability and agility. LEVs have been shown to enhance performance under diverse aspect ratios[8,9] and kinematics.[10–13]

Changes to both the thickness and the camber have a significant influence on the aerodynamic characteristics of the airfoil. Thin wings can create more lift and less drag at low Reynolds numbers,[14] and the location of maximum relative thickness affects the balance among the drag, lift-to-drag ratio, and stall features.[15] In addition, the increased camber elevates the lift coefficient slope and the maximal lift-to-drag ratio of rectangular wings at Reynolds numbers from 10^3 to 10^4.[16] As well as global camber variations,[17–20] local camber adjustments at the leading and/or trailing edge are also effective. Menshchikov and Somov[21] assessed the performance of a morphing airfoil with compliant ailerons and slats through numerical simulations and experimental measurements. Their results show that local camber morphing enhances the lift-to-drag ratio, thereby increasing the operation range and maneuverability. Global camber morphing benefits the lift generation during the delayed stall and wake capture stages by regulating the

development of LEVs.[22] Span morphing has been systematically examined through flat-plate wings with variable span lengths or spanwise oscillations.[23–25] Spanwise morphing or oscillations can enhance the lift by stabilizing the LEVs. Joshi et al.[26] measured the lift histories of pure twist and pure bend morphing wings under accelerating glide conditions. They found that the peak lift can be improved by increasing the local angle of attack and relative speed. Jia et al.[27] found that controlled spanwise bending away from the incoming flow can delay the growth of LEVs by reducing the advection speed of the leading-edge shear layer.

Sweep morphing reconfigures the flow to improve performance, possibly in combination with the other morphing modes described above.[28] Lentink et al.[29] experimentally investigated the glide performance of swifts with long and slender wings (i.e., the hand wing is much longer than the arm wing along the wingspan[30]). Small swept (extended) wings are suitable for slow gliding, while large swept (tucked) wings are superior for fast gliding. Zhang et al.[31] employed direct numerical simulations of separated flows around finite-aspect-ratio swept wings to analyze the wake dynamics under a variety of aspect ratios, angles of attack, and sweep angles. The complexity of the dynamic features of vortex structures was observed to be higher in swept conditions than in unswept conditions. The three-dimensional midspan effects appear and interact with the tip effects, allowing the formation of stationary vortex structures near the wing roots. Additionally, the wake dynamics and aerodynamic characteristics of forward swept wings have been studied[32] with the streamwise vortices in the wake found to stabilize the flow at large forward sweeping angles. Zangeneh[33] utilized the large-eddy simulation framework to reveal the sweep effects on the stability of LEVs over finite-aspect-ratio wings in various pitch motions. The LEV growth was found to be moderated by spanwise vorticity convection and vortex stretching. The sweeping of the wing not only changes the direction of vorticity convection but also prominently increases the magnitude of vorticity convection toward the wingtip. Moreover, sweeping causes a compacted LEV by vortex stretching.

The above investigations have focused on global sweeping, where changes in the leading-edge sweeping angle occupy the total wing from root to tip. Different from global sweeping, local sweeping only modifies the leading-edge sweeping angle over part of the wing span, which is closer to the real planform of natural flyers. Biologically, flying vertebrates morph their wings by moving the forelimbs under musculoskeletal control.[34] The wrist and finger motions drive the sweep morphing in the outboard part of the wings, rather than throughout the total span.[35] Matching this biological structure, multi-jointed flapping is observed and modeled.[36,37] A two-jointed flapping system used to reconstruct the actual kinematics of avian wings is proposed by Liu et al.[38] and then investigated numerically or experimentally by different researchers.[39–41] Local sweep morphing wings with simple kinematics, such as gliding, have inspired the design of new drones that are skilled in maneuverable and efficient flight. The work of Hui et al.[42] shows that pigeon-like drones can employ symmetrical wing morphing to maintain the optimal lift-to-drag ratio under three different Reynolds numbers. Chang et al.[35] developed the PigeonBot drone with soft biohybrid morphing wings, where the real feathers are underactuated by wrist and finger motions. They found that the asymmetric local sweep morphing generated by the asymmetric wrist and/or finger motions can achieve turning maneuvers. Ajanic et al.[43] mimicked the northern goshawk in developing the LisHawk drone. Their flight tests show that local sweep morphing coupled with tail morphing

can enhance maneuverability and agility, modify pitch stability, and reduce power requirements. However, existing research does not provide any insights into local sweep morphing wings under actual kinematics, such as two-jointed flapping and body oscillations. Flying animals flap with the body oscillations, especially those with heavy wings.[44–46] Undulations in lift during flapping flight can produce rapid changes in vertical acceleration, resulting in the vertical oscillating displacement of the body. The effects of such compound motion on aerodynamic performance need to be evaluated to improve our understanding of the vortex dynamics and enable the design of bio-inspired drones (i.e., flapping micro aerial vehicles).

The objective of this study is to investigate local sweep morphing combined with two-jointed flapping and to clarify their effects on aerodynamic performance under the background of vertical body oscillation. In this work, the dynamic sweep morphing of the outer wing is prescribed, accompanied by two-jointed flapping. The vertical oscillating effects of the body are considered by imparting a heaving motion at the wing root. For the aforementioned compound motion, a robust Bayesian optimization method is adopted to determine the kinematic parameters that maximize performance. The remainder of this paper is organized as follows. The flapping and morphing wing model, unsteady flow simulator, and aerodynamic optimization method are described in Sec. II. The effects of two-jointed flapping in local sweep morphing on performance are reported and discussed in Sec. III. Finally, the conclusions of this study are presented in Sec. IV.

II. NUMERICAL MODEL AND METHOD

A. Two-jointed flapping wing with local sweep morphing

The LisHawk drone has an avian-inspired morphing wing and was developed to research the flight capabilities of the northern goshawk.[43] The morphing wing changes the leading-edge sweeping angle of the outboard part by up to 1.48 rad, enabling a maximum span length of 1.05 m. In this work, a morphing wing is modeled to investigate the aerodynamic performance of a two-jointed flapping wing according to the work of Liu et al.[38] The avian wing model is a flat plate consisting of an invariable inner wing $ABDC$ and a variable outer wing $CDFHE$, as shown in Fig. 1(a). The inner wing has a parallelogram outline with a streamwise length of c, spanwise width of b_1, and sweep angle of Λ_1. The baseline shape of the outer wing is formed by a rectangle $CDFE$ and a semi-ellipse FHE. The center of the ellipse R is at the midpoint of line EF, which has a distance of $0.15c$ from the edge CD. The morphing of the outer wing is achieved by changing the sweep angle Λ_2. The span width b_2 of the outer wing is constant during morphing. For a point K on the outer wing, the morphing of the outer wing causes a streamwise displacement. The streamwise displacement is $\Delta x(t) = y_r \tan \Lambda_2(t)$, where y_r is the distance from the point K to the line CD. The length of the chord at any spanwise position is constant during the local sweep morphing. Here, the sweep angle of the inner wing Λ_1 is fixed at -0.35 rad and the sweep angle of the outer wing Λ_2 varies in a reasonable range (see Table I) according to the design of LisHawk.[43] For simplicity, we set $b_1 = b_2 = c$, leading to an aspect ratio (defined as the ratio of the square of the span length to the area of the wing) of 4.40.

The wing model flaps in a flow with velocity U_∞^+ along the x direction. The flapping of the total wing is described by the inner wing elevating angle ψ_1 and the outer wing elevating angle ψ_2 (see Fig. 1),
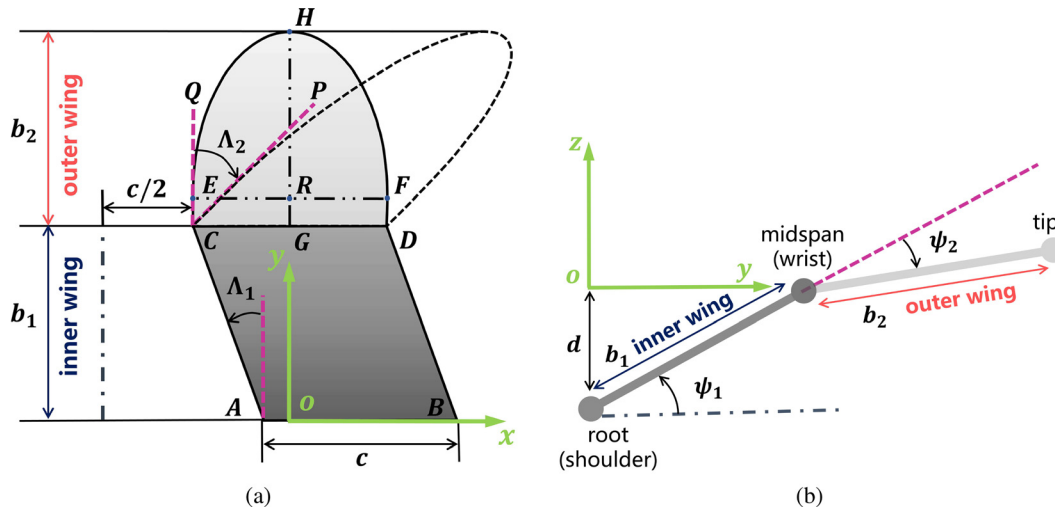
FIG. 1. Schematic diagram of the two-jointed flapping wing in local sweep morphing. (a) Morphing wing model with sweep angles Λ_1 and Λ_2 (for the cases without elevating, $\psi_1 = \psi_2 = 0$). The local sweep morphing is conducted by changing the sweep angle Λ_2. (b) Two-jointed flapping characterized by elevating angles ψ_1 and ψ_2 (zero angle of attack). For the global coordinate system $o - xyz$, the coordinate plane $o - xz$ passes through the root chord AB vertically, and the y-axis crosses the midpoint G of the chord CD.

for which the positive directions are counterclockwise and clockwise, respectively. The elevating motions with respect to time are specified in sinusoidal form as follows:

$$\psi_1(t) = \psi_{10} + \psi_{1m} \sin(2\pi f t), \tag{1}$$

$$\psi_2(t) = \psi_{20} + \psi_{2m} \sin(2\pi f t + \phi_a), \tag{2}$$

where $\psi_{10}(\psi_{20})$ is the average elevating angle of the inner (outer) wing, $\psi_{1m}(\psi_{2m})$ is the elevating amplitude of the inner (outer) wing, and ϕ_a is the phase difference between the elevating of the inner and outer wings. f is the dimensionless flapping frequency, as normalized by the reference frequency $U_\infty{}^+/c$.

The vertical body oscillation induced by the flapping[44] is represented as the heaving motion of the wing root. In the current study, the heaving equation is

$$d(t) = d_m \sin[\psi_1(t)], \tag{3}$$

TABLE I. Setup of the flapping and morphing parameters for the wing model.

Variable	Description	Baseline	Min	Max
ψ_{10} (rad)	Elevating mean of inner wing	0.20	$\cdots$	$\cdots$
ψ_{20} (rad)	Elevating mean of outer wing	0.35	$\cdots$	$\cdots$
ψ_{1m} (rad)	Elevating amplitude of inner wing	0.40	0.35	0.45
ψ_{2m} (rad)	Elevating amplitude of outer wing	0.30	0.25	0.35
ϕ_a (rad)	Phase difference of elevating	0.00	-3.14	3.14
Λ_{20} (rad)	Sweeping mean of outer wing	0.00	-0.30	0.30
Λ_{2m}^* [1]	Normalized sweeping amplitude of outer wing	0.50	0.00	1.00
ϕ_b (rad)	Phase difference of sweeping	0.00	-3.14	3.14
f [1]	Elevating/sweeping frequency	0.24	0.12	0.36

where $d_m = c$ is the heaving amplitude. This heaving motion makes the midspan joint remain at a constant vertical position, as shown in Fig. 1.

Two-jointed flapping also couples with the sweep morphing of the outer wing, which is conducted by manipulating the sweep angle of the outer wing as

$$\Lambda_2(t) = \Lambda_{20} + \Lambda_{2m} \sin(2\pi f t + \phi_b), \tag{4}$$

where Λ_{20} is the average sweep angle of the outer wing, Λ_{2m} is the sweep amplitude of the outer wing, and ϕ_b reflects the phase difference between the elevating and sweeping of the outer wing. In summary, the motion of the two-jointed flapping wing can be determined by nine dimensionless parameters, $(\psi_{10}, \psi_{20}, \Lambda_{20}, \psi_{1m}, \psi_{2m}, \Lambda_{2m}, \phi_a, \phi_b, f)$. The Strouhal number for the flapping flight in this work is computed by $St = f A_m / U_\infty$, where $U_\infty = 1$ is the normalized upstream flow and $A_m = [(b_1 + b_2)/c][\sin(\psi_{10} + \psi_{1m}) - \sin(\psi_{10} - \psi_{1m})]$ is the normalized vertical height swept by the tip of an extended inner wing of length $b_1 + b_2$.

The kinematic parameters are taken from the work of Liu et al.,[38] Taylor et al.,[47] and Ajanic et al.[43] In this study, we estimate the values of the kinematic parameters $(\psi_{10}, \psi_{20}, \psi_{1m}, \psi_{2m})$ by considering the mean value and the first harmonic component in the Fourier series according to the work of Liu et al.[38] The Strouhal number in the range $0.16 < St < 0.62$, including the preferred range of $0.20 < St < 0.40$,[47] is used to bound the elevating and sweeping frequencies $f = St \cdot U_\infty / A_m$. The morphing of the wing is limited by anatomical or physiological constraints. Here, the sweeping angle of the outer wing satisfies $-0.60 < \Lambda_2(t) < 0.60$ rad, namely, $\Lambda_{2m} + |\Lambda_{20}| < 0.60$ rad. To simplify the sampling in the subsequent optimization, we introduce a normalized transformation for the sweeping amplitude. The normalized sweeping amplitude Λ_{2m}^* is equal to $\Lambda_{2m}/(0.60 - |\Lambda_{20}|)$. Consequently, the sweeping parameter space is transformed to be rectangular, as shown in Fig. 2. The baseline and constraints of the
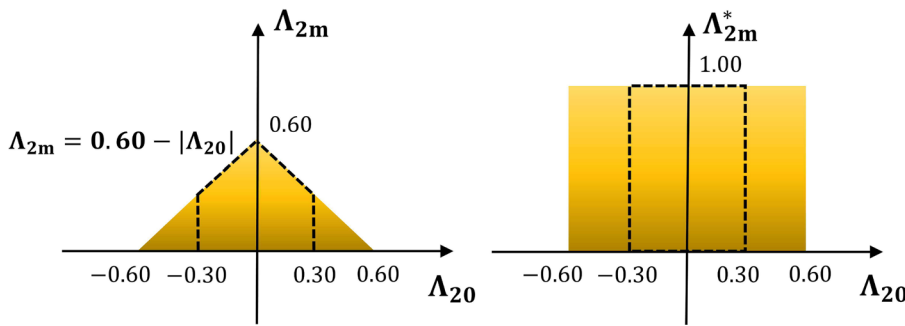
independent kinematic parameters are listed in Table I. The geometric angle of attack (AoA) is fixed at 0.44 rad to form the beneficial separated flow structures observed widely in biological flight.[24]

B. Flow around the two-jointed flapping wing

The flow around the flapping and morphing wing is simulated by numerically solving the time-dependent three-dimensional incompressible Navier–Stokes equations,

$$\nabla \cdot \mathbf{u} = 0, \qquad (5)$$

$$\frac{\partial \mathbf{u}}{\partial t} + \mathbf{u} \cdot \nabla \mathbf{u} = -\nabla p + \frac{1}{\mathrm{Re}} \nabla^2 \mathbf{u} + \mathbf{f}_{\mathrm{IB}}, \qquad (6)$$

where $\mathbf{u}$ is the dimensionless velocity vector, normalized by the reference velocity U_∞^+, p is the dimensionless pressure, normalized by the product of the density ρ and the squared freestream velocity U_∞^{+2}. The Eulerian force density $\mathbf{f}_{\mathrm{IB}}$ represents the effects of the wing model upon the fluid in the immersed boundary method. The Reynolds number is defined as $\mathrm{Re} = U_\infty^+ c / \nu$, where ν is the fluid kinematic viscosity. The simulations in the current study were performed at $\mathrm{Re} = 300$, as in previous studies,[23–25] because the unsteady flow investigated in this work is dominated by the Strouhal number.

We utilize the semi-implicit immersed boundary method in the discrete stream function formulation[48,49] to solve the Navier–Stokes equations on an Eulerian mesh. The spatial discretization is handled by the second-order finite volume method. The time advancement is implemented by the three-step, second-order and low-storage Runge–Kutta scheme. The divergence-free condition is exactly met to machine precision. The convection term and the diffusion term in the momentum equation are solved explicitly and implicitly in each substep, respectively.

The force density $\mathbf{f}_{\mathrm{IB}}$ in Eq. (6) is computed by a Lagrangian direct-forcing approach, where a set of Lagrangian points are employed to represent the geometry and kinematics of the flapping wing. The relation between the force densities on the Eulerian and Lagrangian meshes is given by

$$\mathbf{f}_{\mathrm{IB}}(\mathbf{x}, t) = \int_S \mathbf{F}_{\mathrm{IB}}(\mathbf{X}, t)\delta(\mathbf{x} - \mathbf{X}) dS, \qquad (7)$$

where $\mathbf{X}$ is the spatial coordinates of the Lagrangian mesh. $\mathbf{F}_{\mathrm{IB}}$ is the force density on the Lagrangian mesh. $\delta(\mathbf{x} - \mathbf{X})$ is a Dirac delta function in the three-dimensional space. In numerical simulations, the Dirac delta function $\delta(\mathbf{x} - \mathbf{X})$ is approximated by a regularized delta function $\delta_h(\mathbf{x} - \mathbf{X})$ as follows:

$$\delta_h(\mathbf{x} - \mathbf{X}) = \frac{1}{h^3} \phi\left(\frac{x - X}{h}\right) \phi\left(\frac{y - Y}{h}\right) \phi\left(\frac{z - Z}{h}\right), \qquad (8)$$

where h is the minimum grid width of the Eulerian mesh. (x, y, z) and (X, Y, Z) are the components of the Eulerian position vector $\mathbf{x}$ and Lagrangian position vector $\mathbf{X}$ in the streamwise, spanwise, and vertical directions, respectively. ϕ is a piecewise function,

$$\phi(r) = \begin{cases} \frac{1}{8}\left(3 - 2|r| + \sqrt{1 + 4|r| - 4r^2}\right), & |r| \le 1, \\ \frac{1}{8}\left(5 - 2|r| - \sqrt{-7 + 12|r| - 4r^2}\right), & 1 \le |r| \le 2, \\ 0, & |r| \ge 2. \end{cases} \qquad (9)$$

For a Lagrangian mesh consisting of M points, the force density $\mathbf{F}_{\mathrm{IB}}(\mathbf{X}_j)$ ($j = 1, \dots, M$) on the Lagrangian mesh is computed by

$$\sum_{j=1}^M \left(\sum \delta_h(\mathbf{x} - \mathbf{X}_j)\delta_h(-\mathbf{X}_k)\Delta S h^3 \right) \mathbf{F}_{\mathrm{IB}}(\mathbf{X}_j) = \frac{\Delta \mathbf{U}(\mathbf{X}_k)}{\Delta t}, \qquad (10)$$

where ΔS is the surface area associated with each Lagrangian point. $\Delta \mathbf{U}(\mathbf{X}_k)$ is the difference between the specified velocity boundary condition and the predicted velocity on the Lagrangian point $\mathbf{X}_k$. The force density $\mathbf{F}_{\mathrm{IB}}$ on the Lagrangian mesh is zero when the predicted velocity satisfies the specified boundary condition ($\Delta \mathbf{U} = 0$). Otherwise, the force density on the Lagrangian mesh $\mathbf{F}_{\mathrm{IB}}$ is spread onto the Eulerian mesh for correcting the predicted velocity according to the discretized form of Eq. (7),

$$\mathbf{f}_{\mathrm{IB}}(\mathbf{x}) = \sum_{j=1}^M \mathbf{F}_{\mathrm{IB}}(\mathbf{X}_j)\delta_h(\mathbf{x} - \mathbf{X}_j)\Delta S. \qquad (11)$$

The details of the numerical method can be found in our previous works.[24,48,49] We have validated the numerical method by considering similar moving boundary problems in terms of geometry, kinematics, and Reynolds number.[8,25,50]

The background mesh domain is a large rectangular box with a dimensionless size of $[-6, 12] \times [-9, 9] \times [-9, 9]$ in the streamwise, spanwise, and vertical directions, respectively. The mesh is locally refined to the minimum grid width of $c/40$ to match the average spacing of the mesh modeling the morphing wing. The mesh settings were tested by multiple bio-locomotion cases, and differences in the mesh resolution and domain size were found to have little influence on the average lift and drag coefficients.[24] The boundary conditions of the

computational domain are the uniform freestream condition at the inlet, the free convection condition at the outlet, and the zero-shear free-slip condition on the other four sides. In addition, the non-slip boundary condition is applied on the surface of the flapping and morphing wing. The solution is initialized with a uniform unit streamwise velocity within the computational domain.

The upward lift L and backward drag D are the primary aerodynamic forces determining the flight performance. The force coefficients are defined as

$$C_{L,\tau} = \sum_{\tau}(c_l)_i = \frac{L_\tau}{1/2\rho U_\infty^{+2}S^*}, \tag{12}$$

$$C_{D,\tau} = \sum_{\tau}(c_d)_i = \frac{D_\tau}{1/2\rho U_\infty^{+2}S^*}, \tag{13}$$

where $c_l(c_d)$ is the dimensionless lift (drag) of the ith Lagrange element, S^* is the area of a single wing, and the subscript τ denotes the integral domain. Specifically, "iw" and "ow" denote the domains of the inner wing and the outer wing, respectively. τ is represented as "tw" for the total wing, i.e., the sum of "iw" and "ow."

The pitch moment coefficient M_y and the average position $(\overline{x_{ac}}, \overline{z_{ac}})$ of the aerodynamic center are used to measure the longitudinal control performance of the flight. These quantities are expressed as

$$M_{y,\tau} = \sum_{\tau}(c_d z_r - c_l x_r)_i, \tag{14}$$

$$\overline{x_{ac},\tau} = \frac{\int_T \sum_{\tau}(c_l x_r)_i dt}{\int_T C_{L,\tau}dt}, \tag{15}$$

$$\overline{z_{ac},\tau} = \frac{\int_T \sum_{\tau}(c_d z_r)_i dt}{\int_T C_{D,\tau}dt}, \tag{16}$$

where $x_r(z_r)$ is the streamwise (vertical) coordinate of the ith Lagrange element in the integral domain τ with respect to the reference line (dashed–dotted line) in Fig. 1. The reference line of the pitch moment and the aerodynamic center is parallel to the y-axis and has a streamwise position, c, and a vertical position, h. The integral time T is the dimensionless flapping and morphing period. The average quantities are marked by overlines.

C. Aerodynamic optimization

The current work explores the performance enhancement mechanism underlying the flapping and morphing motion using an efficient global optimization method. The lift is closely related to important performance indicators.[51,52] The aerodynamic optimization problem can be formulated in terms of an objective function and the design vector. In this work, the objective function is taken as the mean lift acting on the total wing (combination of the inner wing and outer wing) $\overline{C_{L,tw}}$ as that in Ref. 53. The design vector is taken as $\xi = [\psi_{1m}, \psi_{2m}, \Lambda_{20}, \Lambda_{2m}^*, \phi_a, \phi_b, f]^T$, which consists of the elevating amplitude of the inner wing ψ_{1m}, the elevating amplitude of the outer wing ψ_{2m}, the sweeping mean of the outer wing Λ_{20}, the normalized sweeping amplitude of the outer wing Λ_{2m}^*, the phase difference of elevating ϕ_a, the

phase difference of sweeping ϕ_b, and the elevating/sweeping frequency f. We adopt the Bayesian optimization method[54,55] with a hybrid acquisition strategy to maximize the average lift coefficient of the total wing $\overline{C_{L,tw}}$. Here, the Gaussian process is used as the probabilistic surrogate model to provide the best evaluation of the objective function and the uncertainty of this evaluation. The generation of the Gaussian process depends on the initial dataset sampled by the optimal Latin hypercube technique.[56]

The process of searching for the optimum conditions and refining the surrogate model is driven by maximizing the acquisition function $\alpha(\xi)$. The acquisition functions are the probability of improvement $\alpha_{PI}(\xi)$, expected improvement $\alpha_{EI}(\xi)$, and upper confidence bound $\alpha_{UCB}(\xi)$. To improve the robustness of the optimization method, we utilize the portfolio $A(\xi) = \{\alpha_{PI}^j(\xi), \alpha_{EI}^j(\xi), \alpha_{UCB}^j(\xi)\}(j = 1, 2, 3)$, reflecting the hybrid acquisition strategy. Specifically, three acquisition functions are involved, and each is assigned three different balance parameters. According to the accumulated gains regulated by the memory factor, the best infill point is suggested from nine candidates during the iteration phase. Additionally, the infill process can be toggled to manual mode to introduce problem-specific expert knowledge.[57] More details of the Bayesian optimization method are given in Refs. 25 and 55.

III. RESULTS AND DISCUSSION

Typical parameter configurations of the two-jointed flapping wing with local sweep morphing are summarized in Table II. The kinematics of the flight depends on the elevating amplitudes ψ_{1m} and ψ_{2m}. The zero amplitude corresponds to gliding flights, while nonzero amplitudes lead to flapping flights. The baseline configuration is used to compare the gliding (Baseline-GM) and two-jointed flapping (Baseline-FM) of the morphing wing. Moreover, the advantages of two-jointed flapping with local sweep morphing are elucidated through the optimal configuration (Optimum-FM).

A. Enhanced performance of two-jointed flapping over gliding

Figure 3 shows the angular parameters and aerodynamic performance over a flapping and morphing period for the baseline configuration (Baseline-FM) of the two-jointed flapping wing with local sweep morphing. The white and gray backgrounds denote the upstroke and downstroke of the inner wing, respectively. The local sweeping has an amplitude of 0.30 rad. For the two-jointed flapping, the amplitude of the inner wing is 30% larger than that of the outer wing. There is no phase difference between the flapping of the inner and outer wings, or between the sweep morphing and flapping of the outer wing. In Fig. 3(b), the lift coefficient of the total wing undulates over the range (0.30, 0.50) in the first half-period, except in the initial

TABLE II. Flapping and morphing parameters of baseline and optimum configurations.

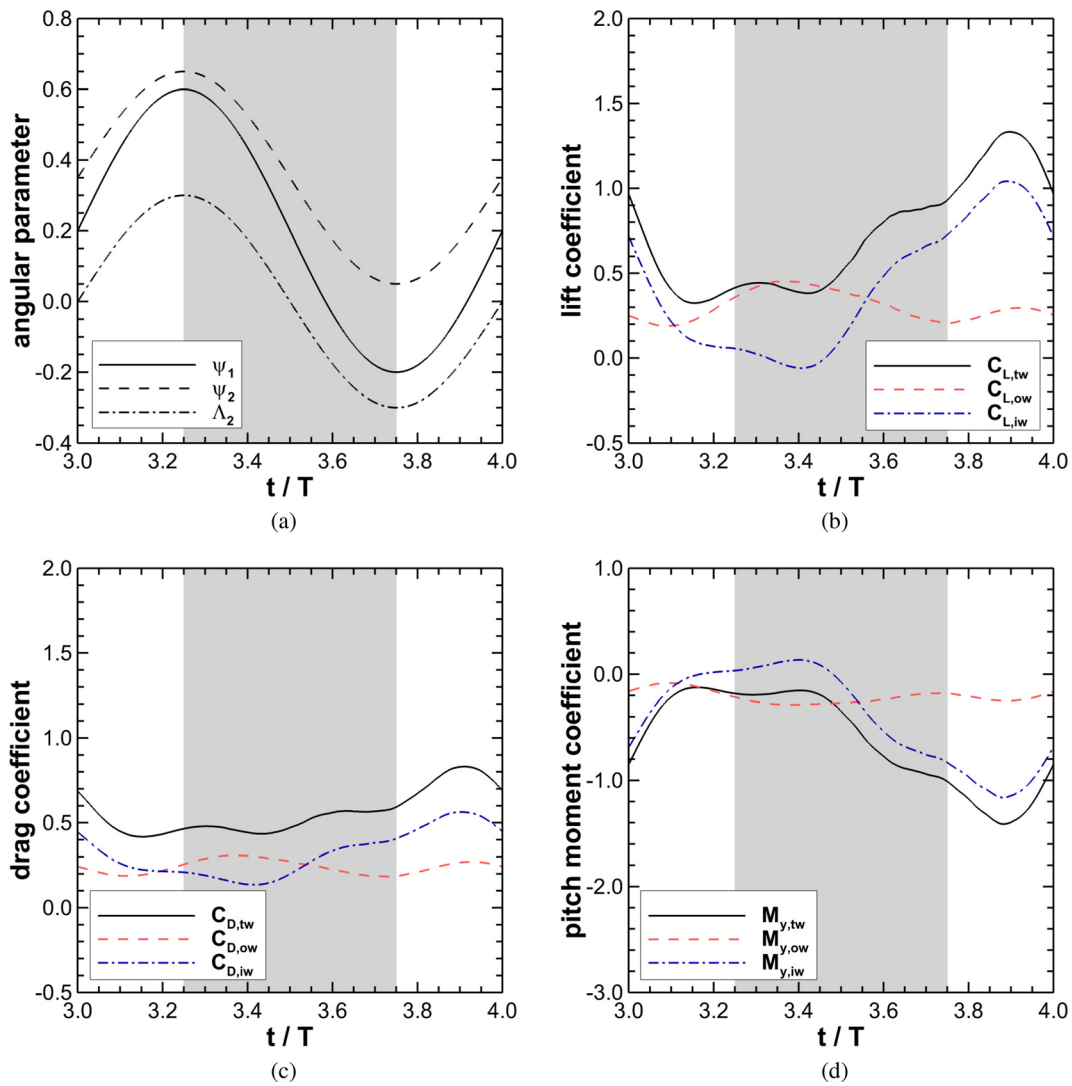| Configuration	ψ_{1m} (rad)	ψ_{2m} (rad)	ϕ_a (rad)	Λ_{20} (rad)	Λ_{2m}^* [1]	ϕ_b (rad)	f [1]
Baseline-FM	0.40	0.30	0.00	0.00	0.50	0.00	0.24
Baseline-GM	0.00	0.00	0.00	0.00	0.50	0.00	0.24
Optimum-FM	0.45	0.35	2.71	−0.05	0.41	−0.16	0.36

FIG. 3. Angular parameters and aerodynamic performance in a flapping and morphing period for the baseline configuration (Baseline-FM) of the two-jointed flapping wing in local sweep morphing. (a) Angular parameters. (b) Lift coefficient. (c) Drag coefficient. (d) Pitch moment coefficient. The white and gray blocks denote the upstroke and downstroke of the inner wing, respectively.

stage. The lift coefficient $C_{L,tw}$ increases gradually to a maximum of 1.33 at the end of the second half-period and then decreases rapidly. The lift of the total wing can be decomposed into the contributions of the inner and outer wings, i.e., $C_{L,tw} = C_{L,ow} + C_{L,iw}$. In the baseline configuration, the undulation of the lift coefficient $C_{L,ow}$ is weak, and its maximum is only 0.45 in the upstroke of the outer wing. The lift coefficient of the inner wing exhibits a similar trend to that of the total wing, with a maximum of 1.04. The maximal instantaneous lifts of the inner wing and the total wing appear at almost equal moments. Therefore, the inner wing plays a dominant role in the evolution of lift.

The histories of the drag and lift on the same surface display similar features, as shown in Fig. 3(c), except that the drag coefficient has a smaller magnitude and weaker fluctuations than the lift coefficient.

The maximal drag coefficients of the total wing and the inner wing are 0.83 and 0.56, respectively. In Fig. 3(d), the magnitude of the pitch moment coefficient changes with time in a similar manner to the lift and drag coefficients. The magnitude of the moment coefficient $|M_{y,tw}|$ decreases from 0.82 to 0.13 over $0.15T$ and then remains at approximately 0.15 for most of the first half-period. As the flapping motion continues, the magnitude of the moment coefficient $|M_{y,tw}|$ grows significantly, reaching a peak of 1.41. This indicates that two-jointed flapping can promote a remarkable change in the pitch moment. The two-jointed flapping motion further extends the margin of maneuverability based on the high maneuverability introduced by pure sweep morphing.[43]

Figure 4 presents the time-dependent kinematic and aerodynamic parameters over a flapping and morphing period for the
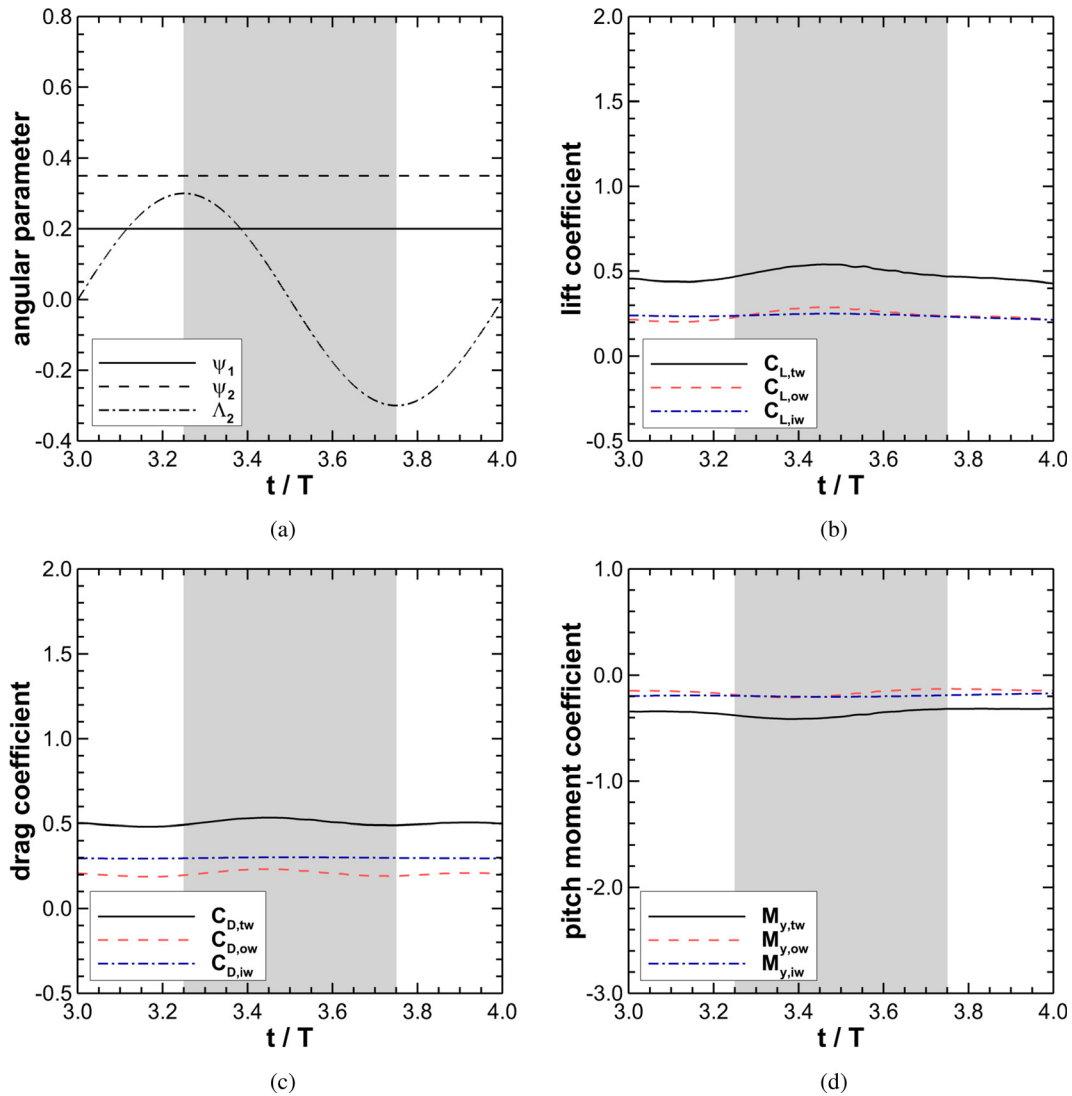
FIG. 4. Angular parameters and aerodynamic performance over a flapping and morphing period for the baseline configuration (Baseline-GM) of the gliding wing with local sweep morphing. (a) Angular parameters. (b) Lift coefficient. (c) Drag coefficient. (d) Pitch moment coefficient. The white and gray blocks denote the backward and forward sweep of the outer wing, respectively.

baseline configuration (Baseline-GM) of the gliding wing with local sweep morphing. The gliding wing undergoes the same change of sweep morphing angle as the two-jointed flapping wing. The elevating angles of the inner and outer wings are fixed at the mean values of the two-jointed flapping wing, i.e., $\psi_1(t) \equiv \psi_{10}$ and $\psi_2(t) \equiv \psi_{20}$. After removing the flapping motion, the aerodynamic forces and moment for both the total wing and the inner/outer wing are almost invariable with respect to time. The lift coefficient of the total wing is about 0.50. The lift coefficients of the inner and outer wings contribute almost equally to the total lift coefficient. The drag coefficient of the total wing is almost equal to the lift coefficient under the gliding condition. Unlike the relationship between lift coefficients, the drag coefficient of the inner wing is greater than that of the outer wing, i.e., $C_{D,iw}(t) \approx 0.30$ and $C_{D,ow}(t) \approx 0.20$. The pitch moment coefficient of the total

wing is about −0.35, and the inner and outer wings make almost equal contributions, namely, $M_{y,iw}(t) \approx M_{y,ow}(t)$.

Table III summarizes the average aerodynamic performance of two-jointed flapping (Baseline-FM) and gliding (Baseline-GM) under

TABLE III. Average aerodynamic performance of baseline and optimum configurations.

Configuration	$\overline{C_{L,tw}}$	$\overline{C_{D,tw}}$	$\dfrac{\overline{C_{L,tw}}}{\overline{C_{D,tw}}}$	$\overline{M_{y,tw}}$	$\overline{x_{ac,tw}}$	$\overline{z_{ac,tw}}$
Baseline-FM	0.72	0.56	1.29	−0.62	0.93	0.08
Baseline-GM	0.48	0.50	0.96	−0.35	0.84	0.09
Optimum-FM	1.40	0.63	2.22	−1.27	1.00	0.21

the baseline configuration. The average lift coefficient of two-jointed flapping is 50% larger than that of gliding. However, there is no significant difference in the average drag coefficients between the two kinds of flight. Accordingly, the average lift-to-drag ratio is 34% higher in the case of two-jointed flapping. We would like to mention that the lift-to-drag ratio here is not used to directly measure the efficiency of the flight, because the "gliding mode" in this work is the gliding of a morphing wing (dynamically changing the sweep angle of the outer wing during the gliding). Additional power is required to account for the morphing wing in the "gliding mode." The "gliding mode" is obtained by turning off the elevating motion from the "flapping mode." The elevating motion of the wing increases both lift and drag. However, the increment of the average lift coefficient is larger than that of the average drag coefficient for the flapping wing model. Here, we employ the lift-to-drag ratio to measure the difference between the increase of lift and drag.

We computed the lift-to-drag ratios for the conventional "gliding mode," where both the elevating motion and sweeping motion are turned off from the "flapping mode." The sweep angle of the conventional "gliding mode" is fixed at $\Lambda_2 = 0.00$, which is the average sweep angle of the corresponding "flapping mode." As shown in Table IV, two conventional gliding configurations are set with different angles of attack of 0.17 and 0.44 rad, respectively. The setup of the angle of attack $AoA = 0.44$ rad inherits from that in the "flapping mode," where the geometric angle of attack $AoA = 0.44$ rad corresponds to a stroke angle of 1.13 rad that falls within the scope of animal flapping flight.[58–60] The setup of the angle of attack $AoA = 0.17$ rad is close to the moderate angle of attack in animal gliding flight.[20] The lift-to-drag ratio of the conventional "gliding mode" at the angle of attack of $AoA = 0.44$ rad is 0.94, which is a little lower than that of the "gliding mode" with dynamically changing the sweep angle of the outer wing. The difference in the lift-to-drag ratio between the two configurations means that the dynamically changing sweep angle of the outer wing during the gliding helps to slightly enhance the lift-to-drag ratio. The lift-to-drag ratio of the conventional "gliding mode" at the angle of attack of $AoA = 0.17$ rad is 1.13, which is higher than that of the conventional "gliding mode" at the angle of attack of $AoA = 0.44$ rad. The lift-to-drag ratio increases as the angle of attack decreases from 0.44 to 0.17 rad, which is consistent with the results of Taira and Colonius[8] The lift-to-drag ratios for all the configurations investigated in this work are of the order of $O(1)$, which is close to the results reported in the work at similar Reynolds numbers.[8,31,32,61] The low lift-to-drag ratio indicates the inferior gliding performance for the configurations investigated in this work. The inferior gliding performance might be caused by the low Reynolds number since a low Reynolds number of 300 is used in this work to ensure the resolution for the flows near the

wing. The Reynolds number used in this work falls in the low Reynolds number region according to the work of Lissaman,[62] where the maximum lift-to-drag ratio of airfoils varies from $O(1)$ to $O(100)$ when the Reynolds number varies from the low Reynolds number region to high Reynolds number region. The effect of the Reynolds number should be carefully investigated when the conclusions on the lift-to-drag ratio are applied to the flight at high Reynolds numbers.

Additionally, the pitch moment coefficient of two-jointed flapping increases by 77% in magnitude compared with that of gliding. These results show that the maneuverability and agility of two-jointed flapping are greater than the corresponding gliding performance for the same local sweep morphing wing. The average position of the aerodynamic center can be computed using Eqs. (15) and (16). The streamwise position $\overline{x_{ac,tw}}$ of the aerodynamic center is 0.93 for two-jointed flapping and 0.84 for gliding. Because of the more downstream position, two-jointed flapping has an advantage over gliding in terms of flight stability.

B. Optimal two-jointed flapping with local sweep morphing

For the local sweep morphing wing, two-jointed flapping enhances longitudinal maneuverability, agility, and stability. The performance can be further improved with reasonable manipulation of the motion parameters. In this subsection, we optimize the flapping and morphing parameters to enhance the average lift of the total wing.

The time dependence of the optimal angular parameters and aerodynamic performance is shown in Fig. 5. Under the optimal configuration (Optimum-FM), the elevating amplitudes of the inner wing and the outer wing are 0.45 and 0.35 rad, respectively. The outer wing leads the inner wing by $0.43T$ in terms of the elevating phase. The sweeping amplitude of the outer wing is 0.23 rad. The sweep morphing of the outer wing lags the elevating of the inner wing by $0.03T$. As exhibited in Fig. 5(b), the lift coefficient of the total wing reaches a minimum of -0.59 at $t = 3.10T$. The lift coefficient $C_{L,tw}$ increases continuously to its maximum of 2.89 at $t = 3.56T$. There is a local maximum of 1.71 at $t = 3.91T$ in the second half-period. The lift coefficient $C_{L,iw}$ of the inner wing remains at a lower level of approximately zero in the first half-period and then grows to a maximum of 1.88 at a similar time to that of the baseline configuration. Overall, the lift coefficient $C_{L,iw}$ exhibits similar trends before and after optimization, which implies that there may be a similar interaction between the inner wing and its surrounding flow. In contrast, the outer wing is subjected to different lift phenomena. The lift coefficient $C_{L,ow}$ is positive in the wide interval from $t = 3.15T$ to $t = 3.72T$. The maximum lift coefficient $C_{L,ow}$ is 2.38 at $t = 3.46T$. The lift enhancement of the outer wing dominates the optimal effect of the total wing.

The smaller drag coefficient $C_{D,tw}$ of the total wing reaches its peak of 1.10 in advance, i.e., at $t = 3.31T$ in the first half-period. This occurs in the interval when $C_{D,ow}$ has a greater effect than $C_{D,iw}$, as shown in Fig. 5(c). The pitch moment coefficient $M_{y,tw}$ presents obvious variations under the optimal configuration. Its magnitude has two distinct peaks. The peak $|M_{y,tw}| = 2.50$ at $t = 3.61T$ is attributed to the component $|M_{y,ow}|$ of the outer wing, while the peak $|M_{y,tw}| = 2.06$ at $t = 3.90T$ is mainly due to the component $|M_{y,iw}|$ of the inner wing.

The average aerodynamic performance between the baseline and optimal configurations is compared in Table III. The optimized average lift coefficient $\overline{C_{L,tw}}$ and average pitch moment coefficient $\overline{M_{y,tw}}$

TABLE IV. Average aerodynamic performance of conventional gliding.

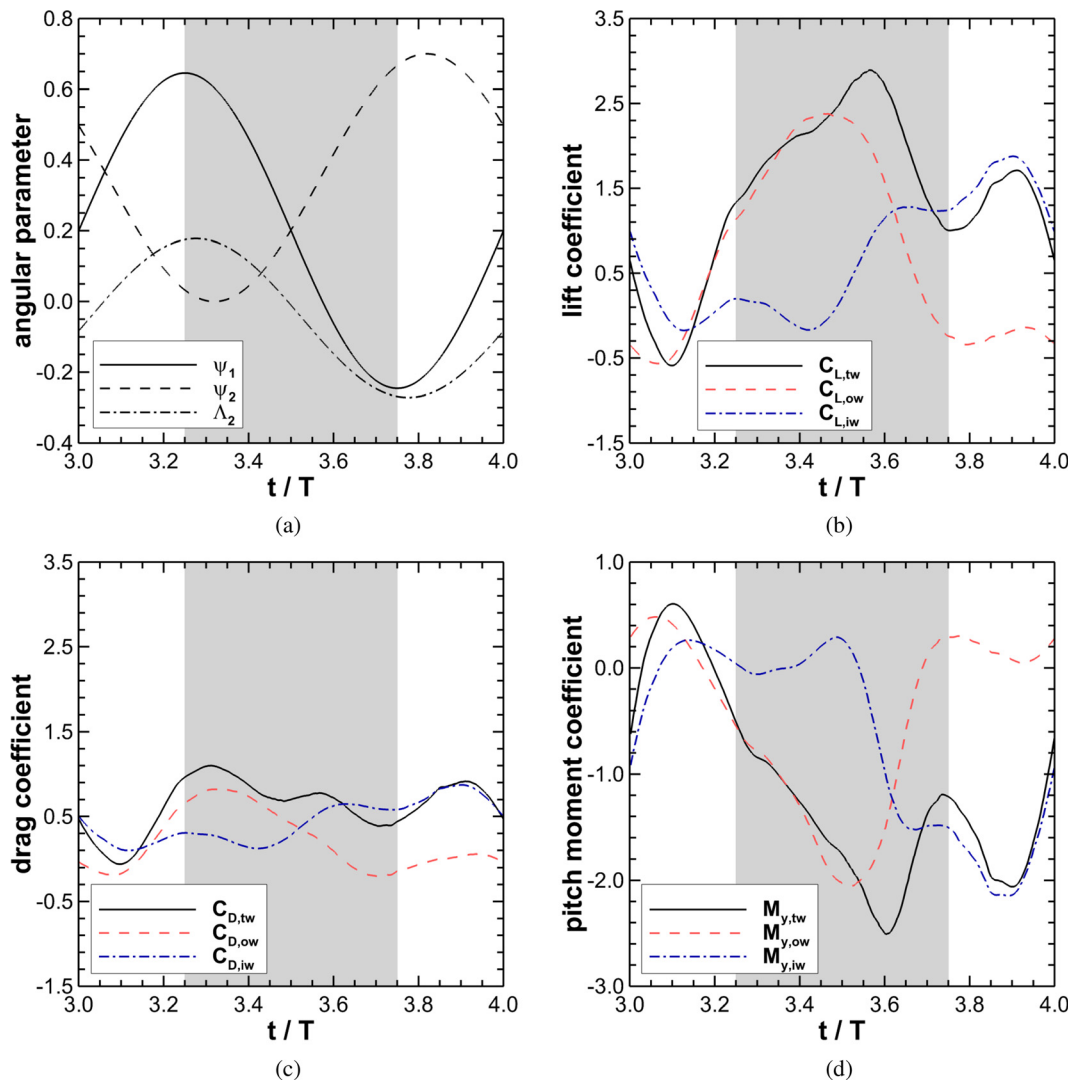| Configuration	$\overline{C_{L,tw}}$	$\overline{C_{D,tw}}$	$\dfrac{\overline{C_{L,tw}}}{\overline{C_{D,tw}}}$
Conventional gliding ($\Lambda_2 = 0.00$, $AoA = 0.44$)	0.48	0.51	0.94
Conventional gliding ($\Lambda_2 = 0.00$, $AoA = 0.17$)	0.33	0.30	1.13

FIG. 5. Angular parameters and aerodynamic performance over a flapping and morphing period for the optimal configuration (Optimum-FM) of the two-jointed flapping wing with local sweep morphing. (a) Angular parameters. (b) Lift coefficient. (c) Drag coefficient. (d) Pitch moment coefficient. The white and gray blocks denote the upstroke and downstroke of the inner wing, respectively.

are approximately twice as large as under the baseline configuration. There is a slight increase by 0.07 in the average drag coefficient $\overline{C_{D,tw}}$. The average lift-to-drag ratio is 1.72 times larger than that of the baseline configuration. The mean streamwise and vertical positions of the aerodynamic center move backward by 0.07 and upward by 0.13, respectively. The increased magnitude of pitch moment coefficient and the shifted aerodynamic center are conducive to flight control. Hence, the optimized two-jointed flapping wing with local sweep morphing achieves improved aerodynamic performance.

C. Vortex structures and vortex force

The combination of two-jointed flapping and local sweep morphing produces a complex flow pattern characterized by the interaction between the inner and outer wings, as shown in Fig. 6. LEVs, trailing-edge vortices (TEVs), and tip vortices (TVs) attach to the edges of the wing, as in many common flapping motions. The two-jointed flapping modifies the vortex structures under the static forward sweep of the inner wing and the dynamic sweep morphing of the outer wing. For convenience, the subscripts "iw" and "ow" represent the vortex structures formed on the inner and outer wings, respectively. The flapping of the inner wing produces LEV_{iw}, which are not uniformly distributed along the spanwise direction. The size of the vortices in the outer section is larger than that in the inner section. Specifically, the complex motion of the outer wing splits the mature LEVs of the outer wing into LEV_{ow} and one unique vortex (riding the chord line near the midspan), which is referred to as the midspan vortex (MSV). Overall, LEV_{iw}, LEV_{ow}, and the MSV constitute a T-shaped branched
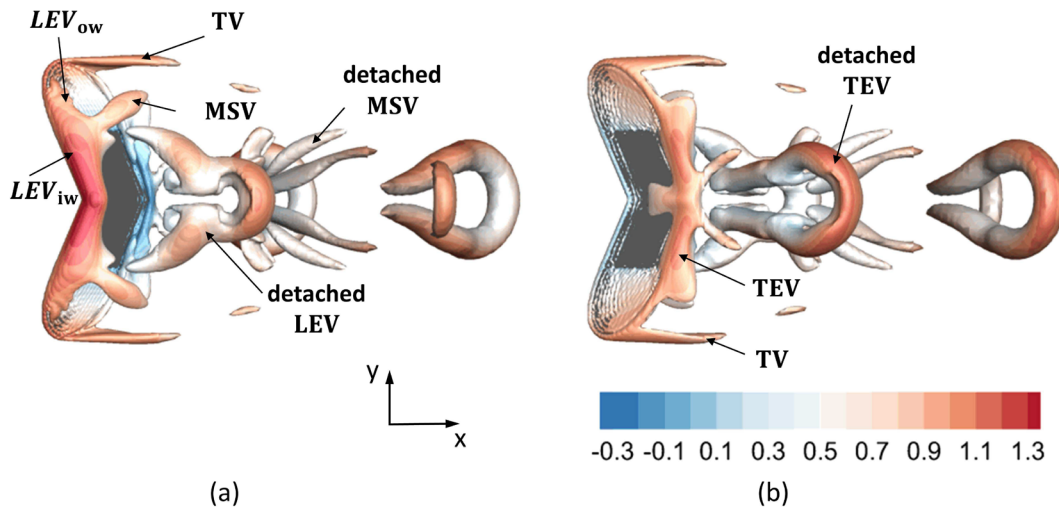
FIG. 6. Three-dimensional flow structures around the flapping and morphing wing under the baseline configuration (Baseline-FM). (a) Top view. (b) Bottom view. The vortex structures are identified with the Q-criterion[8] of 0.75. The isosurface is colored by the streamwise velocity.

structure, which is the main feature of the two-jointed flapping wing with local sweep morphing. A similar branched structure exists at the trailing edge, as shown in Fig. 6(b). The new branch is small and is positioned closer to the wing root. The spanwise vorticity above the outer wing is released through the shedding of the MSV. In contrast, the spanwise vorticity over the inner wing is released through the formation of a hairpin-shaped sub-vortex, as shown in Fig. 7. The hairpin-shaped sub-vortex originates from the detached LEVs from the inner wing. The LEVs detach from the inner wings at the end of the downstroke ($t/T = 2 + 3/4$ in Fig. 7). The detached LEVs are stretched along the streamwise direction as they are advected downstream ($t/T = 3$ to $3 + 1/2$ in Fig. 7). The stretching of the detached LEVs along the streamwise direction turns the spanwise vortices to

streamwise vorticity, which produces two streamwise vortices in the form of hairpin "legs" ($t/T = 3 + 1/2$ in Fig. 7).

Figure 8 shows a schematic of the attached vortex system on the two-jointed flapping wing with local sweep morphing, qualitatively describing the distribution of the vortex system. Because of the relative motion between the inner wing and the outer wing, the MSV carries part of the spanwise vorticity away from the original LEV and turns its axis line downstream. The MSV and the TV on the same side have identical vorticity directions. Nevertheless, the directions of their axis lines are different.

Figure 9 shows the evolution of the vortex system around the flapping and morphing wing over a flapping period. At the initial moment of the period, there is sufficient accumulation of spanwise
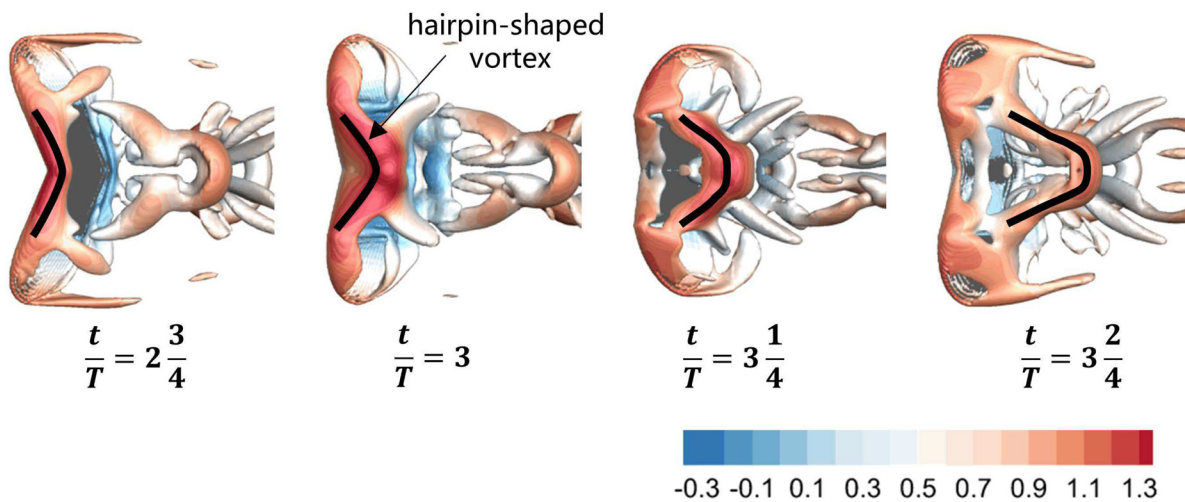

FIG. 7. Evolution of the hairpin-shaped vortex during $(2 + 3/4)T < t < (3 + 2/4)T$ in the baseline configuration (Baseline-FM). The isosurface of $Q = 0.75$ is colored by the streamwise velocity.
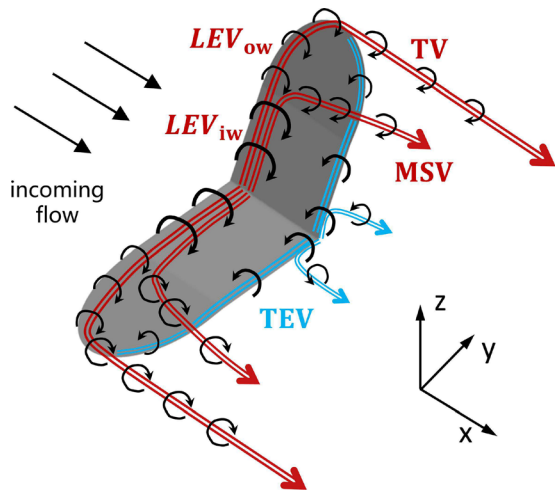
FIG. 8. Schematic of the attached vortex system on the two-jointed flapping wing with local sweep morphing.

vorticity in the LEV of the inner wing, and vortex shedding can be observed. The LEV of the outer wing attaches to the upper surface with a flat shape. In the first half-period, from $3T$ to $(3 + 1/2)T$, the LEV is gradually shed from the inner wing. The new LEV of the inner wing, which carries a small amount of spanwise vorticity, absorbs energy from the mainstream and grows continuously with the flapping. The LEV of the outer wing is stretched along the streamwise direction and becomes flatter with the forward sweep morphing of the outer wing. The LEV is torn because it cannot follow the rapidly morphing outer wing. At the same time, another new LEV begins to be generated on the leading-edge line of the outer wing, and the vorticity required to form the MSV is laid on the wing surface. In the second half-period after $(3 + 1/2)T$, the LEV of the inner wing continues to strengthen. In addition, the LEV of the outer wing also grows, while the MSV moves along the spanwise direction toward the wing root and merges with the LEV of the inner wing. This process further strengthens the LEV of the inner wing. The MSV plays an auxiliary role in stabilizing the LEV of the inner wing. This is due to the fact that the current inner wing can be considered a low-aspect-ratio wing, and the MSV serves as its TV.[8] Therefore, the LEV of the inner wing
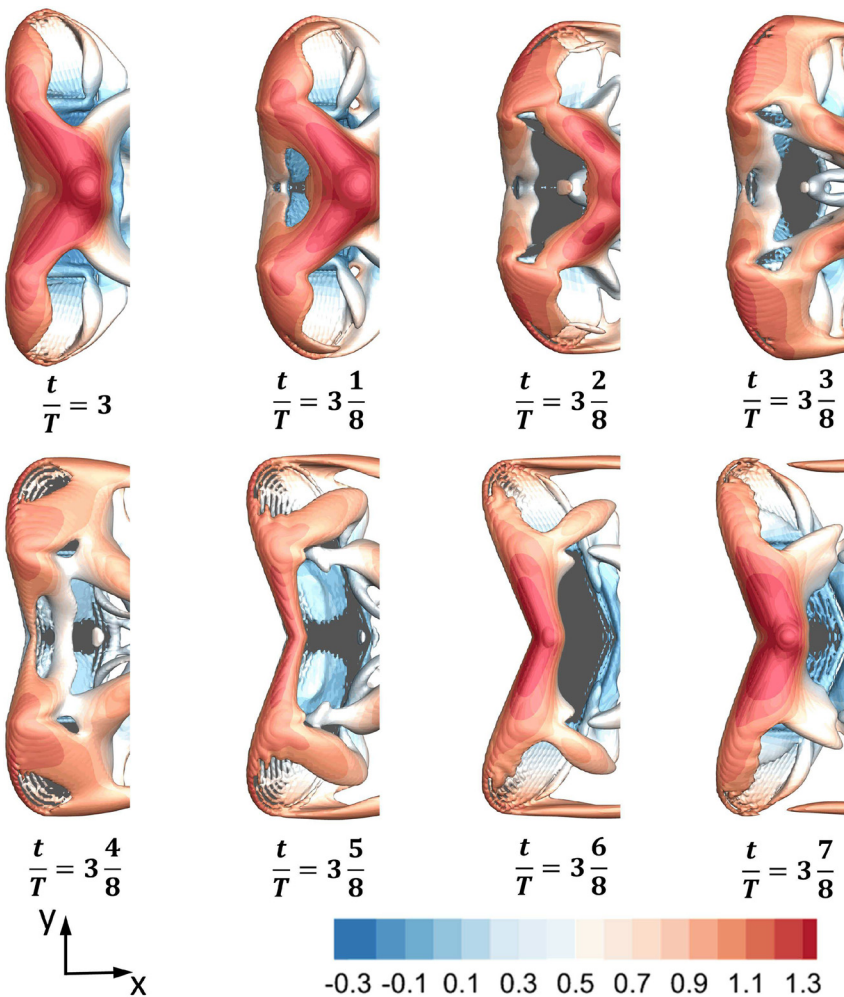

FIG. 9. Evolution of vortex structures around the two-jointed flapping wing over a flapping period under the baseline configuration (Baseline-FM). The isosurface of $Q = 0.75$ is colored by the streamwise velocity.

becomes much stronger and generates higher lift around the end of the period, which is consistent with the lift characteristics in Fig. 3(b).

The vortex force created by the vortex system can be evaluated by the integral of the Lamb vector,[24,25]

$$\boldsymbol{\lambda} = \mathbf{u} \times \boldsymbol{\omega}, \tag{17}$$

where $\boldsymbol{\omega} = \nabla \times \mathbf{u}$ is a dimensionless vorticity vector normalized with U_∞^+/c. The vertical component λ_z of the Lamb vector is $u_x\omega_y - u_y\omega_x$, measuring the vortex lift. Figure 10 shows the distributions of the Lamb vector component λ_z and its decomposed variables in four sections at different spanwise positions. The component λ_z

consists of the variable $u_x\omega_y$ and the variable $-u_y\omega_x$. The variable $u_x\omega_y$ dominates the component λ_z because the variable $-u_y\omega_x$ has much smaller values, as shown in Fig. 10(b). Furthermore, the variable $u_x\omega_y$ expresses the contribution of the spanwise vorticity ω_y [see Fig. 10(d)], representing the LEV, to the vortex lift. Similar distributions of $u_x\omega_y$ and the Lamb vector component λ_z indicate that the LEV dominates the vortex lift. It can be observed that the LEV of the inner wing attaches to the upper surface closer to the LEV of the outer wing in Fig. 10(d).

As shown in Fig. 11(a), gliding leads to a different attached vortex system from two-jointed flapping. The LEVs of the inner and outer wings are flat sheets stretching along the flow direction, with no
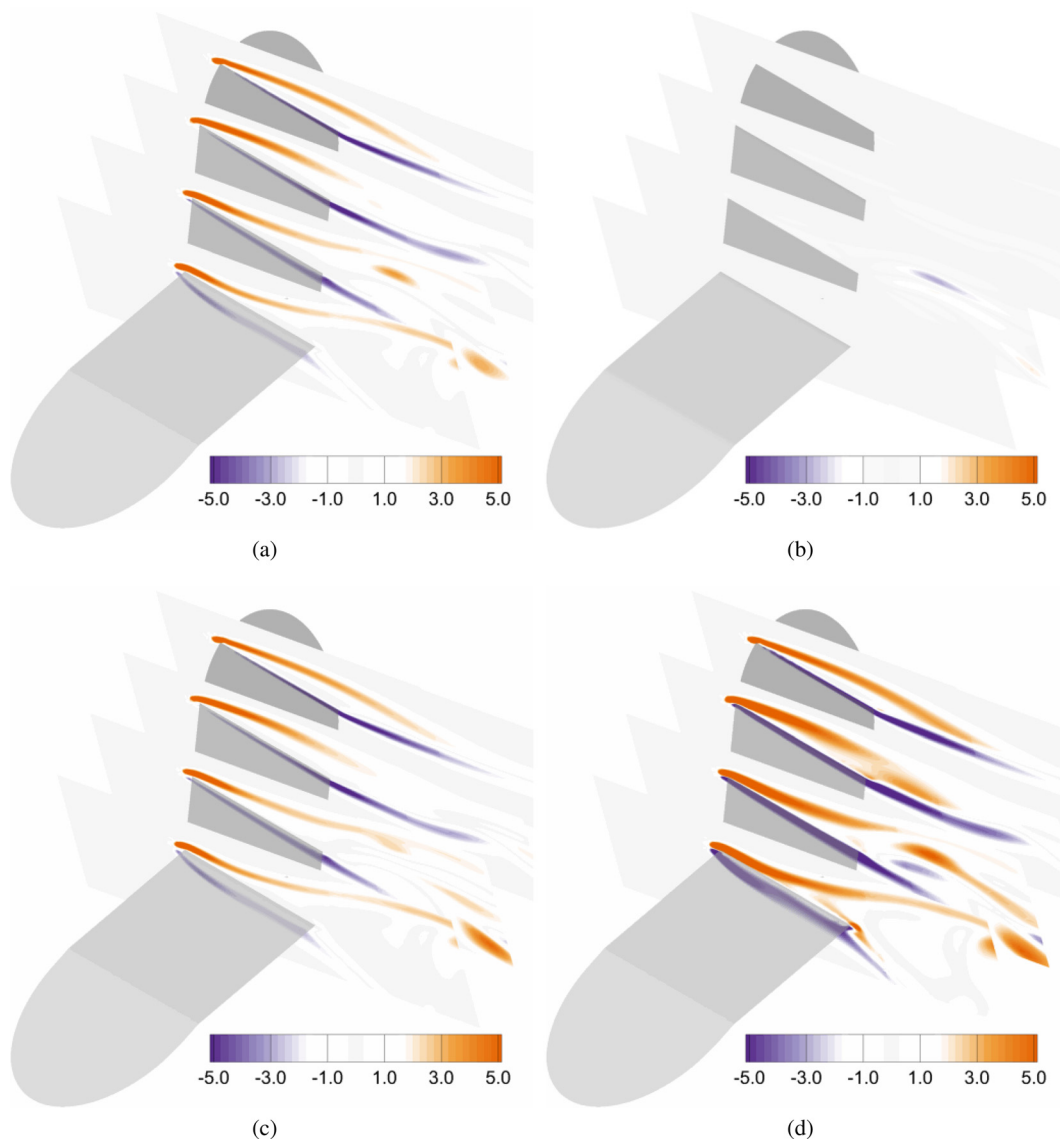

FIG. 10. Lamb vector component $\lambda_z = u_x\omega_y - u_y\omega_x$ and its decomposition in four sections at $t/T = 3 + 5/8$ under the baseline configuration of the two-jointed flapping wing. (a) $u_x\omega_y$. (b) $-u_y\omega_x$. (c) $u_x\omega_y - u_y\omega_x$. (d) Spanwise vorticity ω_y. Each subplot includes four sections at spanwise positions of $y = 0.0$, $y = 0.5$, $y = 1.0$, and $y = 1.5$.
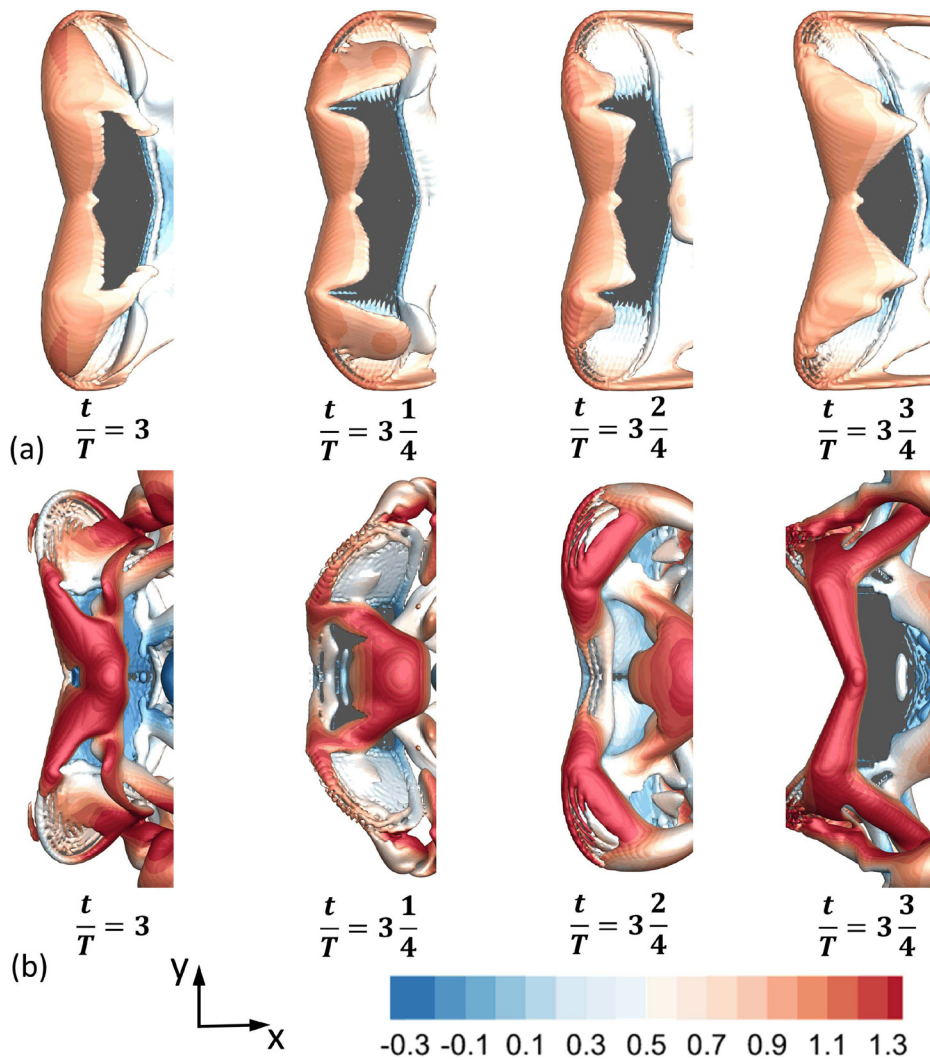
FIG. 11. Evolution of vortex structures in a flapping period under (a) baseline configuration (Baseline-GM) for gliding and (b) optimum configuration (Optimum-FM) for two-jointed flapping. The isosurface of $Q = 0.75$ is colored by the streamwise velocity.

obvious spiral shape. There is a spatial boundary between the LEVs, and no effective MSV appears at the boundary. The slightly fluctuating curves in Figs. 4(b)–4(d) indicate that the forces on the gliding and morphing wing are not sensitive to changes in the vortices. In Fig. 11(b), the flow pattern under the optimum configuration is similar to that in the baseline configuration, albeit with greater unsteadiness. In particular, the LEV of the outer wing produces a secondary bifurcation due to the faster morphing rate of the outer wing later in the period. Additionally, the increase in flapping frequency compared with the baseline configuration increases the relative velocity between the incoming flow and the wing tip by a factor of 1.40. In this work, the cross section of the wing is a thin flat plate, where flow separation occurs at the leading-edge point of the wing. The separation point is independent of the Reynolds number. Therefore, we assume that the aerodynamic forces are dominated by the Strouhal number and wing morphology. However, the Reynolds number effect might affects the

forces in flapping flight. It is worth investigating the effects of the Reynolds number in future work.

Figure 12(a) shows the distributions of the spanwise vorticity ω_y and the Lamb vector component λ_z under the baseline configuration for gliding (Baseline-GM). The spanwise vorticity is concentrated in a slender region at the four spanwise positions, which indicates that the LEV on the gliding wing has a thin layered structure. The LEV and the surface fail to enclose the recirculation zone. The Lamb vector component λ_z has a similar distribution to the spanwise vorticity. These features exist throughout the period. The lack of LEV attachment results in the low lift.

As exhibited in Fig. 12(b), the optimal configuration for two-jointed flapping makes the LEVs of the inner and outer wings attach more tightly to the upper surface than the baseline configuration. In addition, the spanwise vorticity has a larger magnitude and wider distribution, which indicates stronger LEVs under the optimal
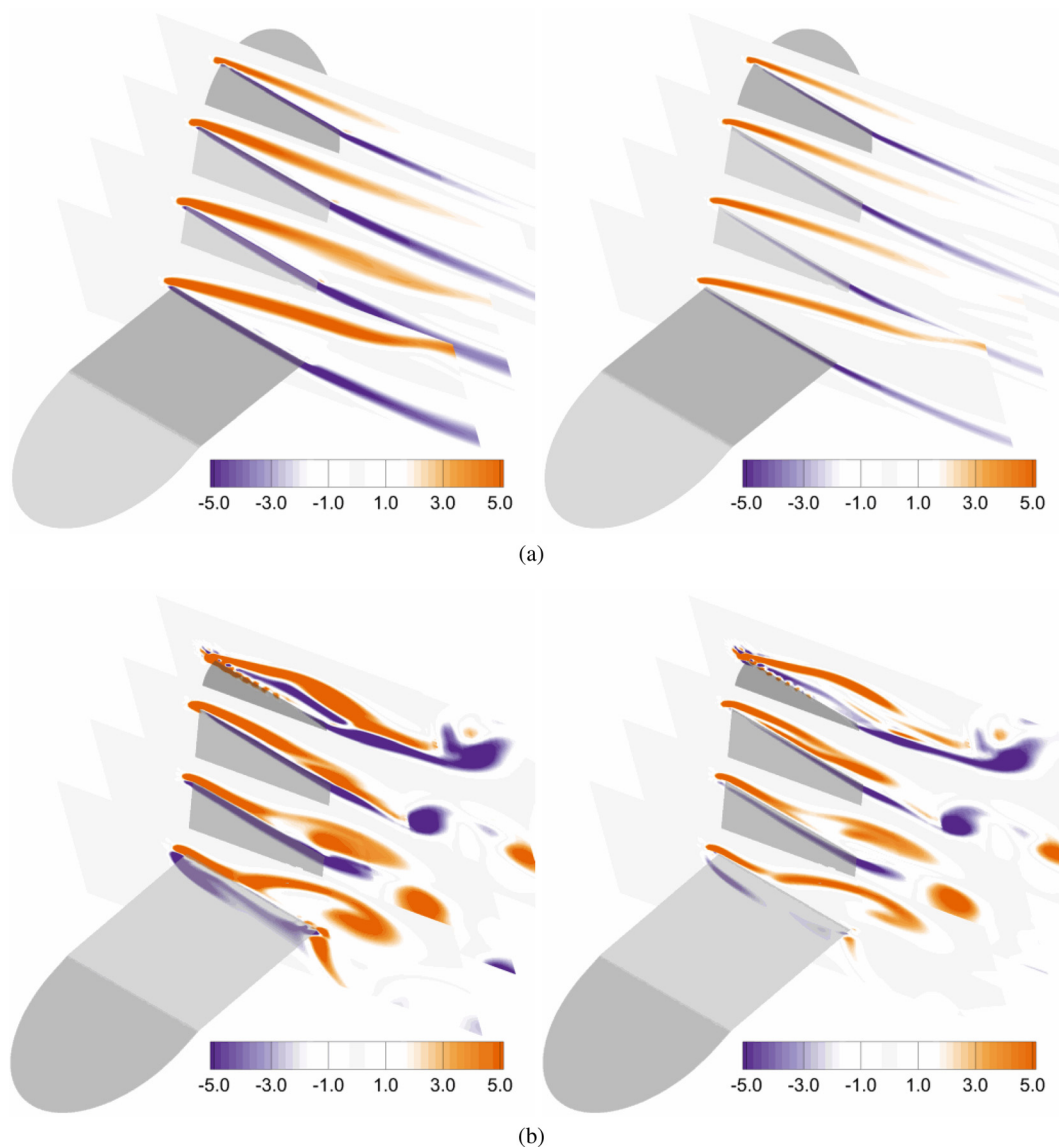
FIG. 12. Spanwise vorticity ω_y (left) and Lamb vector component λ_z (right) in four sections at $t/T = 3 + 5/8$. (a) Baseline configuration for gliding (Baseline-GM). (b) Optimum configuration for two-jointed flapping. Each subplot includes four sections at spanwise positions of $y = 0.0$, $y = 0.5$, $y = 1.0$, and $y = 1.5$.

configuration. These characteristics are also demonstrated in the Lamb vector component λ_z. Therefore, the strength and stability of the LEVs have been optimized to generate higher vortex lift.

Figure 13 displays the attached vortex system and the vortex lift concentration zone, clarifying the generation of the maximum instantaneous lift under the optimal configuration. The lift peaks of the outer wing and the total wing occur at around $t/T = 3 + 1/2$ [see Fig. 5(b)]. The MSV has just formed on the outer wing and its end intersects with the TV. The main part of the MSV becomes attached to the upper surface of the outer wing, and there is a large angle between the MSV axis and the flow direction. The large inclination of the MSV means that it enhances the lift in a similar way to the LEV of the outer wing.

The combination of the MSV and the LEV of the outer wing allows the outer wing to gain much higher vortex lift, as can be seen from the vortex lift concentration zone in Fig. 13(b).

IV. CONCLUSION

The aerodynamic performance of a bio-inspired two-jointed flapping wing with local sweep morphing has been investigated by numerically solving the incompressible Navier–Stokes equations. We compared the lift coefficient, drag coefficient, pitch moment coefficient, and average aerodynamic center position of the two-jointed flapping wing and a counterpart gliding wing. The average lift coefficient of the two-jointed flapping wing was found to be 1.50 times that of the
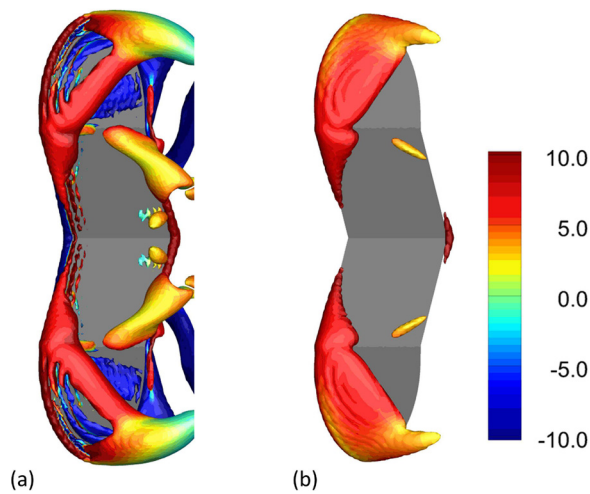
FIG. 13. Attached vortex structures and vortex lift concentration zone at $t/T = 3 + 1/2$ under the optimum configuration (Optimum-FM). (a) Isosurface of $Q = 10.0$. (b) Isosurface of $\lambda_z = 10.0$. The isosurfaces are colored by the spanwise vorticity.

gliding wing under the same local sweep morphing. Two-jointed flapping enhances the average lift-to-drag ratio by a factor of 1.34, which indicates that the increase in the average lift coefficient is larger than that in the average drag coefficient. The magnitude of the pitch moment coefficient increases by 77%, and the aerodynamic center moves backward by 0.09 chord length, which indicates that two-jointed flapping also has significant advantages over gliding in terms of the maneuverability/agility and stability of flight. The unique vortex structures around the two-jointed flapping wing are MSVs, which originate from the LEV of the inner wing. The MSVs interact with the LEVs on the inner and outer wings. Specifically, the MSVs stabilize the LEVs on the inner wing. The high lift of the total wing in two-jointed flapping flight results from the strong LEV attached to the inner wing. We also optimized the kinematics of combined two-jointed flapping and local sweep morphing. The optimal kinematics allows the outer wing to capture the MSV. Consequently, the average lift coefficient of the optimized combined motion is approximately twice that under the baseline configuration. The results presented in this paper reveal the vortex structures and physics underlying the enhanced performance of a combined two-jointed flapping wing and local sweep morphing, shedding light onto the dynamics of such configurations.

ACKNOWLEDGMENTS

AUTHOR DECLARATIONS
Conflict of Interest

The authors have no conflicts to disclose.

DATA AVAILABILITY

The data that support the findings of this work are available from the corresponding author upon reasonable request.

REFERENCES

[1]D. Li, S. Zhao, A. Da Ronch, J. Xiang, J. Drofelnik, Y. Li, L. Zhang, Y. Wu, M. Kintscher, H. P. Monner *et al.*, "A review of modelling and analysis of morphing wings," Prog. Aerosp. Sci. **100**, 46–62 (2018).

[2]R. M. Ajaj, C. S. Beaverstock, and M. I. Friswell, "Morphing aircraft: The need for a new design philosophy," Aerosp. Sci. Technol. **49**, 154–166 (2016).

[3]M. Hassanalian, A. Quintana, and A. Abdelkefi, "Morphing and growing micro unmanned air vehicle: Sizing process and stability," Aerosp. Sci. Technol. **78**, 130–146 (2018).

[4]L. Chu, Q. Li, F. Gu, X. Du, Y. He, and Y. Deng, "Design, modeling, and control of morphing aircraft: A review," Chin. J. Aeronaut. **35**, 220–246 (2022).

[5]A. Sofla, S. Meguid, K. Tan, and W. Yeo, "Shape morphing of aircraft wing: Status and challenges," Mater. Des. **31**, 1284–1292 (2010).

[6]J. D. Eldredge and A. R. Jones, "Leading-edge vortices: Mechanics and modeling," Annu. Rev. Fluid Mech. **51**, 75–104 (2019).

[7]W. Shyy and H. Liu, "Flapping wings and aerodynamic lift: The role of leading-edge vortices," AIAA J. **45**, 2817–2819 (2007).

[8]K. Taira and T. Colonius, "Three-dimensional flows around low-aspect-ratio flat-plate wings at low Reynolds numbers," J. Fluid Mech. **623**, 187–207 (2009).

[9]H. Ben-Gida, R. Gurka, and D. Weihs, "Leading-edge vortex as a high-lift mechanism for large-aspect-ratio wings," AIAA J. **58**, 2806–2819 (2020).

[10]X. G. Meng and M. Sun, "Aerodynamics and vortical structures in hovering fruit flies," Phys. Fluids **27**, 031901 (2015).

[11]C. Hefler, R. Noda, H. Qiu, and W. Shyy, "Aerodynamic performance of a free-flying dragonfly—A span-resolved investigation," Phys. Fluids **32**, 041903 (2020).

[12]L. Wang, L.-H. Feng, Y. Liang, Y.-L. Chen, and Z.-Y. Li, "Vortex control strategy for unsteady aerodynamic optimization of a plunging airfoil at a low Reynolds number," Phys. Fluids **33**, 117110 (2021).

[13]D. Zhang, Q.-G. Huang, G. Pan, L.-M. Yang, and W.-X. Huang, "Vortex dynamics and hydrodynamic performance enhancement mechanism in batoid fish oscillatory swimming," J. Fluid Mech. **930**, A28 (2022).

[14]W. Thielicke and E. J. Stamhuis, "The influence of wing morphology on the three-dimensional flow patterns of a flapping wing at bird scale," J. Fluid Mech. **768**, 240–260 (2015).

[15]D. Ma, Y. Zhao, Y. Qiao, and G. Li, "Effects of relative thickness on aerodynamic characteristics of airfoil at a low Reynolds number," Chin. J. Aeronaut. **28**, 1003–1015 (2015).

[16]W. Shyy, Y. Lian, J. Tang, D. Viieru, and H. Liu, *Aerodynamics of Low Reynolds Number Flyers* (Cambridge University Press, 2008).

[17]G.-Y. He, S.-G. Zhang, and X. Zhang, "Thrust generation and wake structure of wiggling hydrofoil," Appl. Mathematics Mech. **31**, 585–592 (2010).

[18]H. Wan, H. Dong, and G. P. Huang, "Hovering hinge-connected flapping plate with passive deflection," AIAA J. **50**, 2020–2027 (2012).

[19]X. Lin, J. Wu, and T. Zhang, "Effect of torsional spring and shape on the performance of bioinspired caudal fin," Phys. Fluids **33**, 071903 (2021).

[20]J. A. Cheney, J. P. Stevenson, N. E. Durston, M. Maeda, J. Song, D. A. Megson-Smith, S. P. Windsor, J. R. Usherwood, and R. J. Bomphrey, "Raptor wing morphing with flight speed," J. R. Soc. Interface **18**, 20210349 (2021).

[21]A. Menshchikov and A. Somov, "Morphing wing with compliant aileron and slat for unmanned aerial vehicles," Phys. Fluids **31**, 037105 (2019).

[22]X. Su, Z. Yin, Y. Cao, and Y. Zhao, "Numerical investigations on aerodynamic forces of deformable foils in hovering motions," Phys. Fluids **29**, 041902 (2017).

[23]S. Wang, X. Zhang, G. He, and T. Liu, "Lift enhancement by dynamically changing wingspan in forward flapping flight," Phys. Fluids **26**, 061903 (2014).

[24]S. Wang, G. He, and X. Zhang, "Lift enhancement on spanwise oscillating flat-plates in low-Reynolds-number flows," Phys. Fluids **27**, 061901 (2015).

[25]C. Wang, Z. Xu, X. Zhang, and S. Wang, "Optimal reduced frequency for the power efficiency of a flat plate gliding with spanwise oscillations," Phys. Fluids **33**, 111908 (2021).

[26]K. Joshi, C. G. Vazquez, J. L. Kauffman, and S. Bhattacharya, "Unsteady maneuvering of a morphing wing," in *AIAA Scitech 2020 Forum* (AIAA, 2020), p. 0333.

[27]K. Jia, T. Scofield, M. Wei, and S. Bhattacharya, "Vorticity transfer in a leading-edge vortex due to controlled spanwise bending," Phys. Rev. Fluids **6**, 024703 (2021).

[28]B. Parslew, "Predicting power-optimal kinematics of avian wings," J. R. Soc. Interface **12**, 20140953 (2015).

[29]D. Lentink, U. Müller, E. Stamhuis, R. de Kat, W. van Gestel, L. Veldhuis, P. Henningsson, A. Hedenström, J. J. Videler, and J. L. van Leeuwen, "How swifts control their glide performance with morphing wings," Nature **446**, 1082–1085 (2007).

[30]P. Henningsson, L. C. Johansson, and A. Hedenström, "How swift are swifts *Apus apus*?," J. Avian Biol. **41**, 94–98 (2010).

[31]K. Zhang, S. Hayostek, M. Amitay, A. Burtsev, V. Theofilis, and K. Taira, "Laminar separated flows over finite-aspect-ratio swept wings," J. Fluid Mech. **905**, R1 (2020).

[32]K. Zhang and K. Taira, "Laminar vortex dynamics around forward-swept wings," Phys. Rev. Fluids **7**, 024704 (2022).

[33]R. Zangeneh, "Investigating sweep effects on the stability of leading-edge vortices over finite-aspect ratio pitch-up wings," Phys. Fluids **33**, 107104 (2021).

[34]D. D. Chin, L. Y. Matloff, A. K. Stowers, E. R. Tucci, and D. Lentink, "Inspiration for wing design: How forelimb specialization enables active flight in modern vertebrates," J. R. Soc. Interface **14**, 20170240 (2017).

[35]E. Chang, L. Y. Matloff, A. K. Stowers, and D. Lentink, "Soft biohybrid morphing wings with feathers underactuated by wrist and finger motion," Sci. Rob. **5**, eaay1246 (2020).

[36]T. Wolf and R. Konrath, "Avian wing geometry and kinematics of a free-flying barn owl in flapping flight," Exp. Fluids **56**, 1 (2015).

[37]A. K. Stowers, L. Y. Matloff, and D. Lentink, "How pigeons couple three-dimensional elbow and wrist motion to morph their wings," J. R. Soc. Interface **14**, 20170224 (2017).

[38]T. Liu, K. Kuykendoll, R. Rhew, and S. Jones, "Avian wing geometry and kinematics," AIAA J. **44**, 954–963 (2006).

[39]J.-S. Maeng, J.-H. Park, S.-M. Jang, and S.-Y. Han, "A modeling approach to energy savings of flying Canada geese using computational fluid dynamics," J. Theor. Biol. **320**, 76–85 (2013).

[40]S. Qin, Z. Weng, Z. Li, Y. Xiang, and H. Liu, "On the controlled evolution for wingtip vortices of a flapping wing model at bird scale," Aerosp. Sci. Technol. **110**, 106460 (2021).

[41]X. Lang, B. Song, W. Yang, and X. Yang, "Effect of spanwise folding on the aerodynamic performance of three dimensional flapping flat wing," Phys. Fluids **34**, 021906 (2022).

[42]Z. Hui, Y. Zhang, and G. Chen, "Aerodynamic performance investigation on a morphing unmanned aerial vehicle with bio-inspired discrete wing structures," Aerosp. Sci. Technol. **95**, 105419 (2019).

[43]E. Ajanic, M. Feroskhan, S. Mintchev, F. Noca, and D. Floreano, "Bioinspired wing and tail morphing extends drone flight capabilities," Sci. Rob. **5**, eabc2897 (2020).

[44]A. E. Pete, D. Kress, M. A. Dimitrov, and D. Lentink, "The role of passive avian head stabilization in flapping flight," J. R. Soc. Interface **12**, 20150508 (2015).

[45]K. Suzuki, I. Okada, and M. Yoshino, "Effect of wing mass on the free flight of a butterfly-like model using immersed boundary–lattice Boltzmann simulations," J. Fluid Mech. **877**, 614–647 (2019).

[46]R. Xu, X. Zhang, and H. Liu, "Effects of wing-to-body mass ratio on insect flapping flights," Phys. Fluids **33**, 021902 (2021).

[47]G. K. Taylor, R. L. Nudds, and A. L. Thomas, "Flying and swimming animals cruise at a Strouhal number tuned for high power efficiency," Nature **425**, 707–711 (2003).

[48]S. Wang and X. Zhang, "An immersed boundary method based on discrete stream function formulation for two-and three-dimensional incompressible flows," J. Comput. Phys. **230**, 3479–3499 (2011).

[49]S. Wang, G. He, and X. Zhang, "Parallel computing strategy for a flow solver based on immersed boundary method and discrete stream-function formulation," Comput. Fluids **88**, 210–224 (2013).

[50]W. Shyy, P. Trizila, C.-K. Kang, and H. Aono, "Can tip vortices enhance lift of a flapping wing?," AIAA J. **47**, 289–293 (2009).

[51]F. T. Muijres, P. Henningsson, M. Stuiver, and A. Hedenström, "Aerodynamic flight performance in flap-gliding birds and bats," J. Theor. Biol. **306**, 120–128 (2012).

[52]H. Liu, T. Nakata, N. Gao, M. Maeda, H. Aono, and W. Shyy, "Micro air vehicle-motivated computational biomechanics in bio-flights: Aerodynamics, flight dynamics and maneuvering stability," Acta Mech. Sin. **26**, 863–879 (2010).

[53]H. Zheng, F. Xie, T. Ji, and Y. Zheng, "Kinematic parameter optimization of a flapping ellipsoid wing based on the data-informed self-adaptive quasi-steady model," Phys. Fluids **32**, 041904 (2020).

[54]T. de P. Vasconcelos, D. A. de Souza, C. L. Mattos, and J. P. Gomes, "No-PASt-BO: Normalized portfolio allocation strategy for Bayesian optimization," in *2019 IEEE 31st International Conference on Tools with Artificial Intelligence (ICTAI)* (IEEE, 2019), pp. 561–568.

[55]C. Wang, Z. Xu, X. Zhang, and S. Wang, "Bayesian optimization for the spanwise oscillation of a gliding flat-plate," arXiv:2109.04382 (2021).

[56]R. Yondo, E. Andrés, and E. Valero, "A review on design of experiments and surrogate models in aircraft real-time and many-query aerodynamic analyses," Prog. Aerosp. Sci. **96**, 23–61 (2018).

[57]A. L. Marsden, M. Wang, J. E. Dennis, and P. Moin, "Optimal aeroacoustic shape design using the surrogate management framework," Optim. Eng. **5**, 235–262 (2004).

[58]B. W. Tobalske and K. P. Dial, "Flight kinematics of black-billed magpies and pigeons over a wide range of speeds," J. Exp. Biol. **199**, 263–280 (1996).

[59]B. W. Tobalske, W. L. Peacock, and K. P. Dial, "Kinematics of flap-bounding flight in the zebra finch over a wide range of speeds," J. Exp. Biol. **202**, 1725–1739 (1999).

[60]M. Wolf, L. C. Johansson, R. von Busse, Y. Winter, and A. Hedenström, "Kinematics of flight and the relationship to the vortex wake of a Pallas' long tongued bat (*Glossophaga soricina*)," J. Exp. Biol. **213**, 2142–2153 (2010).

[61]K. Zhang, S. Hayostek, M. Amitay, W. He, V. Theofilis, and K. Taira, "On the formation of three-dimensional separated flows over wings under tip effects," J. Fluid Mech. **895**, A9 (2020).

[62]P. Lissaman, "Low-Reynolds-number airfoils," Annu. Rev. Fluid Mech. **15**, 223–239 (1983).